Contents

Text S1-S10
Figures S1-S10
Tables S1-S2

Text S1: Simplified Hydraulics Model

The purpose of our study is to ascertain the characteristic transit time of mud in the Yukon River. To achieve this goal, we build on prior sediment budget approaches, employing transit length scales and residence timescales. For our values to best characterize the long-term sediment transport behavior, we opt to use available historical gage data, rather than instantaneous values determined directly from our field observations. To facilitate the use of the historical gage data, we prescribe a data-informed channel-floodplain cross-section, which allows us to calculate the riverbed settling flux and inundated floodplain area as a function of discharge. The calibration of this cross-section is presented in the main text. Additionally, to calculate the overbank deposition flux, we use the floodplain stream tube model presented in Lauer and Parker (2008). Diagrammatic representations of both the stream tube model (Fig. S1a) and the channel-floodplain cross-section (Fig. S1b) are presented below.

Text S2: Wintertime Hydraulics

During the winter, we surveyed the hydraulics through a hole cut in the ice above the channel thalweg. To estimate the total discharge, we combined our unit discharge measurement with previously collected bathymetric data (Fig. S2). From our wintertime fieldwork, we estimate the winter shear stress to be about 0.63 Pa and the surface sediment concentration to be 1.03×10^{-6} $m^3\ m^{-3}$ (SI Table 1). At such low flow conditions, large gravel clasts are below the threshold of incipient motion, suggesting that in the gravel-bedded reach of the Yukon River, fine sediment occluded from the flow (not on the surface or in the pore spaces of the surface gravel layer; Schiller and Strom, 2026) may be effectively locked in place until the subsequent freshet, longer than our calculation predicts. In the sand bedded reach, sand entrainment rates are low and likely dominated by a lethargic bedload flux, supporting the abrupt increase in the riverbed residence time at the onset of the winter.

Text S3: Beaver Pebble Count

As described in the text, our Ponar samples in Beaver did not accurately sample the gravel clasts on the riverbed. To estimate the true bed grain size distribution, we performed pebble counts on five exposed gravel bars during the fall field campaign (Fig. S3).

Text S4: Suspended Sediment Rating Curve

Following standard practice, to estimate the total suspended sediment concentration as a function of discharge, we build a rating curve from historical observations at Pilot Station, AK. However,

the suspended sediment samples were collected from surface waters, which have lower sediment concentrations than deeper waters. Before fitting the rating curve, we estimate the depth-averaged suspended sediment concentration from the surface measurements by multiplying the observations by a factor of 1.66 (Fig. S4).

Text S5: Suspended Sediment Seasonal Observations

On the Koyukuk River, over the four field seasons, the total sediment discharge varied by a factor of ~14, while the mud discharges varied by a factor of 11. In spring 2022, discharge was 2050 $m^3 s^{-1}$, the depth-averaged sediment concentration was 1.55 x 10^{-4} $m^3 m^{-3}$, and the depth-averaged mud content was 0.78, therefore, the total and mud suspended sediment discharges were 0.32 $m^3 s^{-1}$ and 0.25 $m^3 s^{-1}$, respectively. In the fall, the discharge (1216 $m^3 s^{-1}$), sediment concentration (5.86 x 10^{-5} $m^3 m^{-3}$), and mud content (0.68) all dropped relative to the spring, resulting in a decreased total suspended sediment discharge (0.07 $m^3 s^{-1}$), as well as mud discharge (0.05 $m^3 s^{-1}$). In spring 2023, within-channel discharge was 3197 $m^3 s^{-1}$, the suspended sediment concentration was 1.90 x 10^{-4} $m^3 m^{-3}$, and the mud fraction was 0.66. The total suspended sediment discharge was 0.60 $m^3 s^{-1}$, while the mud suspended sediment discharge was 0.40 $m^3 s^{-1}$. Finally, in fall 2023, discharge was 1124 $m^3 s^{-1}$, the depth-averaged sediment concentration was 3.92 x 10^{-5} $m^3 m^{-3}$, and the depth-averaged mud content was 0.82. The total and mud discharges were determined to be 0.044 $m^3 s^{-1}$ and 0.036 $m^3 s^{-1}$, respectively.

On the Yukon River near Beaver, the total and mud suspended sediment discharge varied by factors of 10 and 8, respectively. In spring 2022, discharge was 10271 $m^3 s^{-1}$, depth-averaged sediment concentration was 1.42 x 10^{-4} $m^3 m^{-3}$, and the mud fraction was 0.93; the total suspended sediment discharge was 1.46 $m^3 s^{-1}$, while the mud discharge was 1.36 $m^3 s^{-1}$. Subsequently, discharge (4879 $m^3 s^{-1}$), sediment concentration (4.27 x 10^{-5} $m^3 m^{-3}$), and mud content (0.85) all dropped in the fall. We determined the total and mud suspended sediment discharges to be 0.21 $m^3 s^{-1}$ and 0.18 $m^3 s^{-1}$, respectively. In spring 2023, discharge was 8762 $m^3 s^{-1}$, the suspended sediment concentration was 2.28 x 10^{-4} $m^3 m^{-3}$, and the mud content was 0.61. Therefore, the total suspended sediment discharge was 2.00 $m^3 s^{-1}$ and the mud suspended sediment discharge was 1.21 $m^3 s^{-1}$. In the fall of 2023, discharge (5204 $m^3 s^{-1}$) and sediment concentration (3.91 x 10^{-5} $m^3 m^{-3}$) dropped relative to the spring, but the mud content increased (0.81). We calculated the total and mud suspended sediment discharges to be 0.20 $m^3 s^{-1}$ and 0.16 $m^3 s^{-1}$. At Wide River, the total and mud suspended sediment discharge varied by factors of 27 and 26 over the three measured seasons. In spring 2022, discharge was 4667 $m^3 s^{-1}$, the depth-averaged sediment concentration was 2.06 x 10^{-4} $m^3 m^{-3}$, and the mud content was 0.84. The total suspended sediment discharge was 0.96 $m^3 s^{-1}$ and the mud suspended sediment discharge was 0.80 $m^3 s^{-1}$. In the fall of that year, the discharge (1783 $m^3 s^{-1}$), sediment concentration (4.26 x 10^{-5} $m^3 m^{-3}$), and mud content (0.71) all decreased relative to the spring. We determined the total and mud suspended sediment discharges to be 0.08 $m^3 s^{-1}$ and 0.05 $m^3 s^{-1}$, respectively. In spring 2023, we did not conduct suspended sediment sampling in Wide River, but the discharge was 5606 $m^3 s^{-1}$. Lastly, in fall 2023, discharge was 1301 $m^3 s^{-1}$, sediment concentration was 2.68 x

10^{-5} m^3 m^{-3}, and the mud content was 0.90. We calculated the sediment discharges (total and mud) to be 0.035 m^3 s^{-1} and 0.031 m^3 s^{-1}, respectively.

In the distributary system of the Yukon River, mud (and total) discharges were far less seasonally variable than in upstream alluvial reaches. For example, in the Yukon River, the total and mud discharges only varied by factors of 2.5 and 2, respectively. In spring 2023, discharge was 8830 m^3 s^{-1} at low tide and 10364 m^3 s^{-1} at high tide, respectively. Depth-averaged suspended sediment concentrations were near identical between tidal phases: 4.26 x 10^{-4} m^3 m^{-3} at low tide and 4.23 x 10^{-4} m^3 m^{-3} at high tide. Similarly, the depth-averaged mud content at low tide (0.79) and high tide (0.75) were very similar. The total and mud suspended sediment discharges were 3.76 m^3 s^{-1} and 2.96 m^3 s^{-1} at low tide, whereas at high tide, the discharges were 4.38 m^3 s^{-1} and 3.30 m^3 s^{-1}, respectively. In the fall, discharge at low tide was 5892 m^3 s^{-1} and 6714 m^3 s^{-1} at high tide. As with the spring, the suspended sediment concentrations (3.81 x 10^{-4} m^3 m^{-3} at low tide and 2.53 x 10^{-4} m^3 m^{-3} at high tide) did not vary greatly between low and high tide, but the mud content increased from 0.77 to 0.93. At low tide, the total and mud suspended discharges were 2.25 m^3 s^{-1} and 1.72 m^3 s^{-1}, respectively. At high tide, the total suspended sediment discharge (1.70 m^3 s^{-1}) and mud suspended sediment discharge (1.59 m^3 s^{-1}) both decreased as a result of the decreased sediment concentration. In the Alakanuk Pass, our observations were similar between the upstream and downstream sites. Seasonally, the total and mud discharges varied by factors of 3 and 2 at both the main and downstream localities. In spring 2023, discharge was 937 m^3 s^{-1} (main) and 986 m^3 s^{-1} (downstream). The suspended sediment concentration was 6.98 x 10^{-4} m^3 m^{-3} (main) and 6.69 x 10^{-4} m^3 m^{-3} (downstream). Lastly, the mud content was 0.70 (main) and 0.57 (downstream). At the main depth-profile site, the total and mud suspended sediment discharges were 0.65 m^3 s^{-1} and 0.46 m^3 s^{-1}, respectively. At the downstream site, the total suspended sediment discharge was 0.66 m^3 s^{-1}, while the mud suspended sediment discharges was 0.37 m^3 s^{-1}. In the fall, discharge was 789 m^3 s^{-1} at the main site and 816 m^3 s^{-1} in the downstream site. The suspended sediment concentration (2.40 x 10^{-4} m^3 m^{-3}) and mud content (0.94) at the main locality were nearly identical to the concentration (2.52 x 10^{-4} m^3 m^{-3}) and mud content (0.92) at the downstream locality. At the main locality, the total suspended sediment discharge was 0.19 m^3 s^{-1} and the mud suspended sediment discharge was 0.18 m^3 s^{-1}. At the downstream location, the total and mud suspended sediment discharges were 0.21 m^3 s^{-1} and 0.19 m^3 s^{-1}, respectively. Finally, in the Kwiguk Pass, the total sediment discharge varied by a factor of 3 and the mud discharge varied by a factor of 2. The springtime discharge was 2310 m^3 s^{-1}, the depth-averaged suspended sediment concentration (4.97 x 10^{-4} m^3 m^{-3}), and the depth-averaged mud content was 0.57. The calculated total and mud suspended sediment discharge were 1.15 m^3 s^{-1} and 0.65 m^3 s^{-1}, respectively. In the fall, discharge (1536 m^3 s^{-1}) and suspended sediment concentration (2.20 x 10^{-4} m^3 m^{-3}) decreased, while the mud content increased (0.95).

Text S6: Point Bar Grain Size Composition Chronosequence

Our bank samples are from the upper portions of point bars, which are generally believed to reflect the upward-fining of lower point bar deposits into the inclined heterolithic strata that cap point bar deposits (McGowen and Garner, 1970; Thomas et al., 1987; Bridge et al., 1995). However, the grain size delineation between these deposits and the underlying homogenous sandy deposits is not always observed (Hartley et al., 2015; Clift et al., 2019) and may be superimposed upon downstream sediment coarsening approaching the meander apex and downstream sediment fining after the apex (Smith et al., 2009; Ghinassi and Ielpi, 2015). In any case, we observe no difference in the deposit mud fraction as a function of age, consistent with both quasi-constant transport conditions on kyr timescales, as well as insignificant in-situ chemical weathering (Fig. S5).

Text S7: Rapid Bank Erosion Observations

During our field campaigns, we observed the erosion of large blocks of bank material (Fig. S6), in accordance with the predictions of previous workers (Douglas et al., 2023).

Text S8: Sediment Transport Time Series

From the discharge time series, we generate a time series of the sediment flux from our calibrated rating curve (Fig. S4). We also generate time series of the hydraulic geometries of flow within the channel, as well as on the floodplain (Fig. S7). Using these time series, we generate time series of the riverbed and overbank settling fluxes (Fig. S8). Additionally, using the calibrated bank erosion model presented in the main text, we generate a time series of the point bar growth flux (Fig. S8).

Text S9: Riverbed Residence Timescale in Relation to Bed Morphodynamics

While the determination of the residence time is sufficient for our calculation, it is useful to examine our formulation in the context of traditional bed morphodynamics, which should explain the relevant phenomena contributing to the riverbed residence timescale. Our formulation of the riverbed residence time treats the entrainment of any individual particle as a random (Poisson) process with equal probability for each particle, which we hypothesize is an appropriate assumption for a turbulent, well-mixed reservoir (i.e., the water column). However, unlike the water column, in the riverbed, the vertical structure of the active layer, bedform morphodynamics, as well as the grain-size-specific transport mode in the near-bed region are all likely relevant with regards to setting the timescale for resuspension. We identify three unique transport histories for sediment entering the near-bed region. Presumably, sediment grains that experience the shortest timescale to resuspension enter the near-bed water column, travel downstream in the near-bed region, and are resuspended without ever interacting with the riverbed. Similarly, sediment could deposit onto the riverbed, experience burial under the thin, saltating bedload layer, but relatively rapidly reenter suspension without translating downstream as bedload, thereby bypassing bedform turnover. Lastly, sediment could deposit onto the riverbed, participate in bedload transport, experience burial in dune troughs (where the minimum

timescale for resuspension becomes the timescale for the dune to migrate approximately one wavelength), and eventually experience resuspension. The first scenario bypasses deposition, the second scenario bypasses dune troughs, and the final scenario is characteristic of classical bedload transport.

We hypothesize that for a given grain size class, the proportions of bed material bypassing classical bedload transport (scenario 2) as compared to the proportion participating in classical bedload transport (scenario 3) sets the riverbed residence time. We test this hypothesis by comparing the grain-size-specific riverbed residence timescales to the dune migration timescale, the time required for a dune to migrate one wavelength. A riverbed residence time shorter than the dune migration timescale suggests that a significant fraction of grain-size-specific bedload transport bypasses dune troughs. On the other hand, if the grain-size-specific riverbed residence time is longer than the dune migration timescale, grains are likely transported as saltating bedload, occasionally suspended into the water column.

We define the dune migration timescale (τ_D; T) as the quotient of the dune area (A_D; L^2) and the per width bedload transport rate (q_b; $L^2\ T^{-1}$),

$$\tau_D = \frac{A_D}{q_b} \quad \text{(eq. S1).}$$

In their review of dune scaling relationships, Bradley and Venditti (2017) documented a strong relationship between dune height and wavelength,

$$H_D = 0.051\,(L_D)^{0.7744} \quad \text{(eq. S2).}$$

Inverting Eq. (S2) to calculate the dune length and assuming a triangular dune shape, we calculate the dune area (A_D) to be 58.6 m^2. Next, we employ a standard bedload flux equation,

$$\frac{q_b}{\sqrt{RgD^3}} = m\,(\tau_* - \tau_{*c})^n \quad \text{(eq. S3),}$$

where submerged specific gravity (R) equals 1.65, g is the gravitational acceleration, m and n are empirical constants, which we set to 5.7 and 1.5, respectively (Fernandez Luque and Van Beek, 1976). The critical Shields number,

$$\tau_{*c} = 0.5\left[0.22Re_p^{-0.6} + 0.06 \cdot 10^{\left(-7.7Re_p^{-0.6}\right)}\right] \quad \text{(eq. S4),}$$

is a function of the particle Reynolds number,

$$Re_p = \frac{\sqrt{RgD}D}{\nu} \quad \text{(eq. S5).}$$

To evaluate Eq. (S3)-(S5), we set the kinematic viscosity of water (ν) equal to 1 x 10^{-6} m^2 s^{-1}, and the grain diameter, D, to 250 x 10^{-6} m, approximately the D_{50} of the Yukon River near Alakanuk, as sampled in the fall of 2023. Lastly, we calculate the Shields number (τ_*) as

$$\tau_* = \frac{\tau_b}{(\rho_s - \rho)\, gD} \quad \text{(eq. S6).}$$

We set the bed shear stress, τ_b equal to 8.26 Pa (the median value measured in the Yukon River during our springtime observations at Beaver and Huslia), calculate the Shields number, the bedload transport rate, and finally arrive at the dune migration timescale (τ_D), which we determine to be 2.61 days. During the ice-free period of the hydrologic year, the riverbed residence timescale typically fluctuates between about 2 and 6 days for mud, whereas for sand the calculated residence time fluctuates between about 7 and 15 days. For sand, we interpret a riverbed residence significantly longer than the dune turnover timescale to be consistent with classical mixed bedload-suspended load transport. For mud, we hypothesize that the similarity between the dune turnover timescale and the riverbed residence time calculation suggests that either sediment cohesion increases the critical shear stress for mud entrainment (Partheniades, 1965), coarser particles bury and occlude mud from the flow (Schiller and Strom, 2026), or flocs can be transported as saltating bedload (de Lange et al., 2024). In other words, mud may behave as either mixed bed-suspended load or as cohesive/occluded suspended load. In either case, evidently, mud can reside in the riverbed active layer.

Text S10: Transit Times for Sand and Unflocculated Mud

In the main text, we primarily focus on our transit time estimates for flocculated mud particles. However, for the model in which we only consider riverbed depositional events, we also determined the transit time of sand particles, as well as mud grains, if they were unflocculated (Fig. S9). The field-derived constants used for the unflocculated mud and sand cases are available in the supplementary data. For the unflocculated mud case, shorter transit times are entirely the byproduct of a longer advection length scale because the riverbed residence time was not adjusted in this case. For sand grains, longer transit times are the result of both shorter advection length scales and longer riverbed residence timescales. For sand, we also determined the transit time distribution using the model that included both riverbed and floodplain deposition (Fig. S10). We found that for sand, nearly all of the particles entered the floodplain at one point during transit, meaning that the floodplain residence time dominated their transit times, although with a significant contribution from riverbed storage.

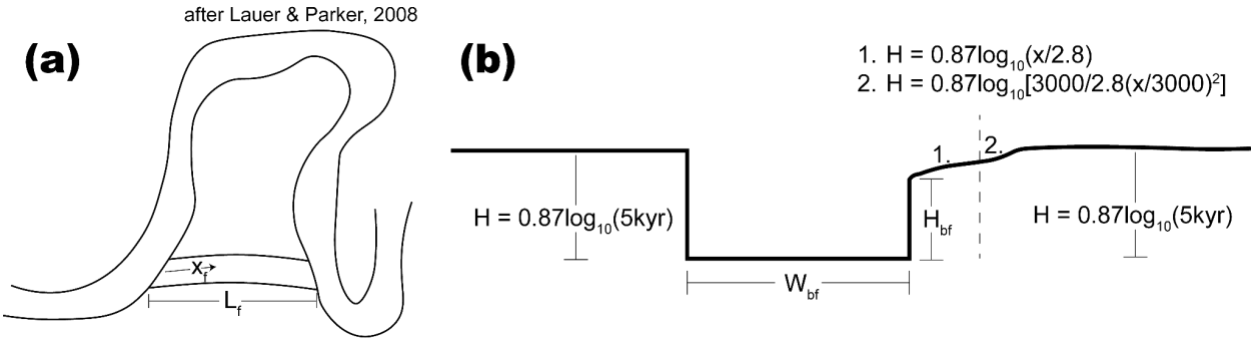


Figure S1: (a) Diagram of the previously developed stream tube schematic used to approximate the length scale of overbank flow paths. Assuming $L_f >> HU/w_i$, we calculate the average overbank deposition rate as $D_{avg} = C_{i,0}UH/L_f$. (b) A simple floodplain-channel complex calibrated to capture the in-channel and overbank discharge and sediment transport dynamics of the Yukon River.

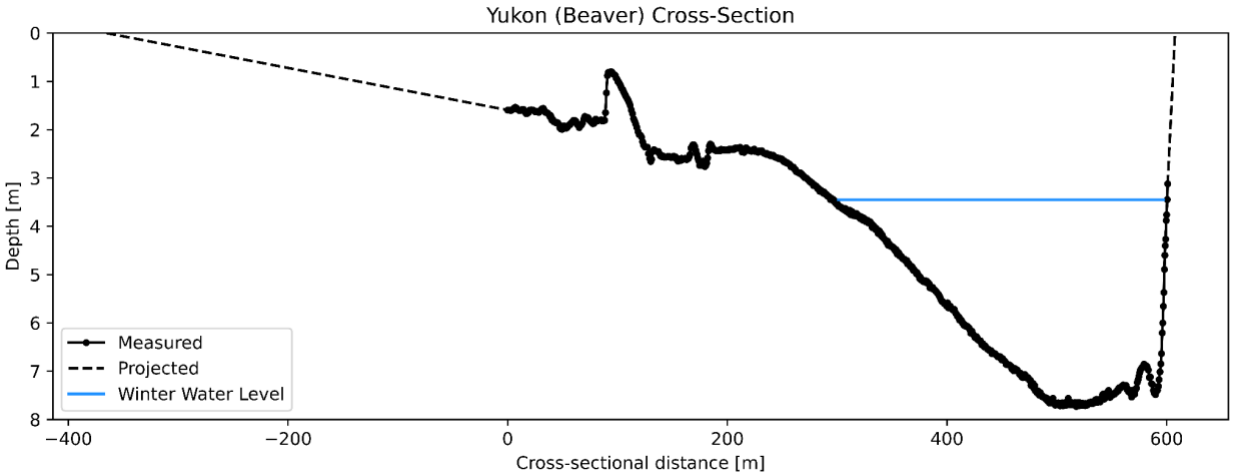


Figure S2: An example of the estimated river cross sectional area during the winter.

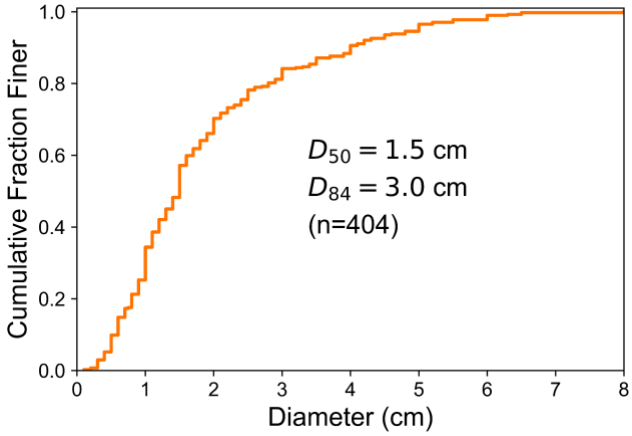


Figure S3: Effective cumulative distribution function (ECDF) of the grain diameter of clasts counted on five exposed gravel bars in the Yukon River near Beaver.

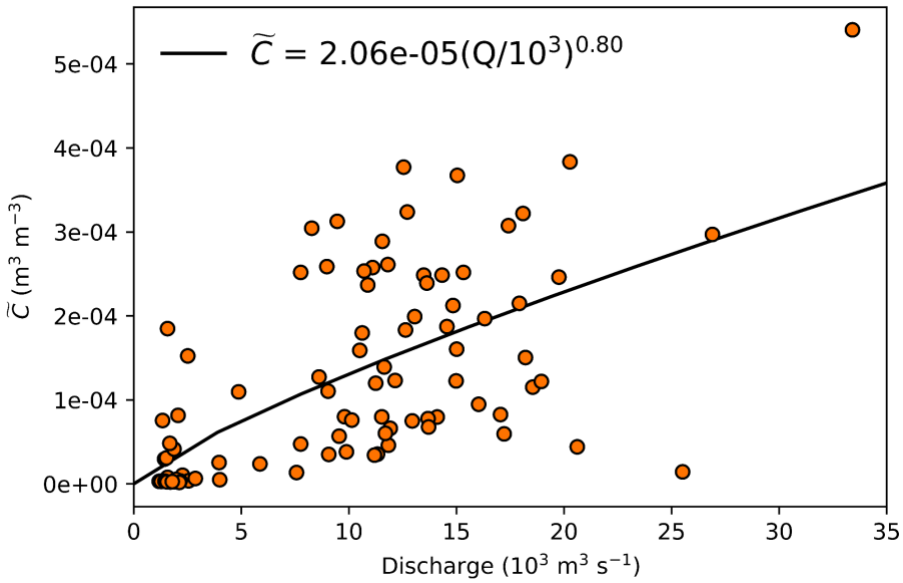


Figure S4: Suspended sediment concentration rating curve developed from the ArcticGRO samples collected at Pilot Station, AK. The depth-averaged sediment concentration was estimated by multiplying the observed surface sediment concentrations by 1.66.

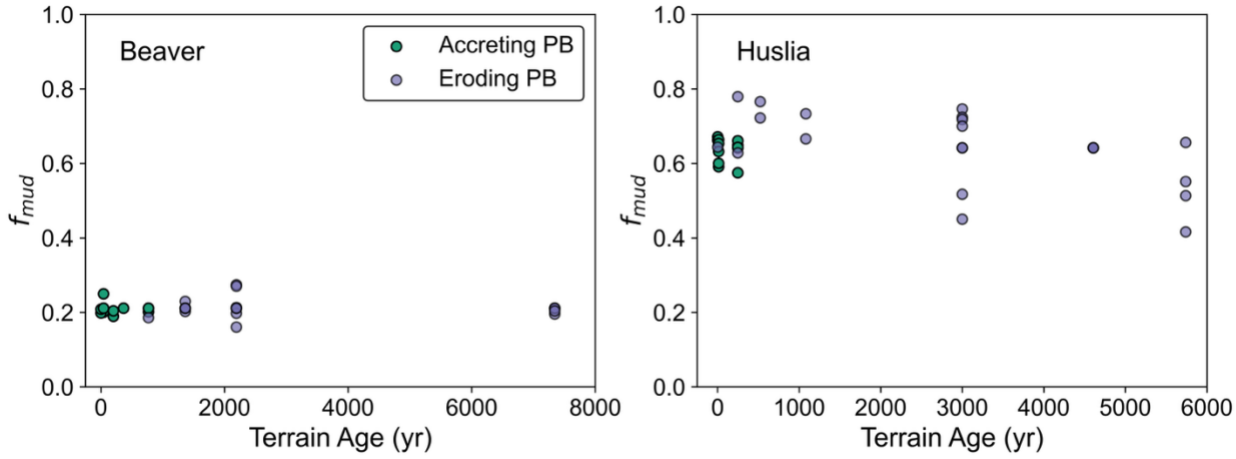


Figure S5: Mud contents of floodplain point bar deposits as a function of terrain age. In both Beaver and Huslia, the mud content in variably aged deposits is indistinguishable from the mud content observed in actively accreting point bars, suggesting no significant in situ chemical denudation.

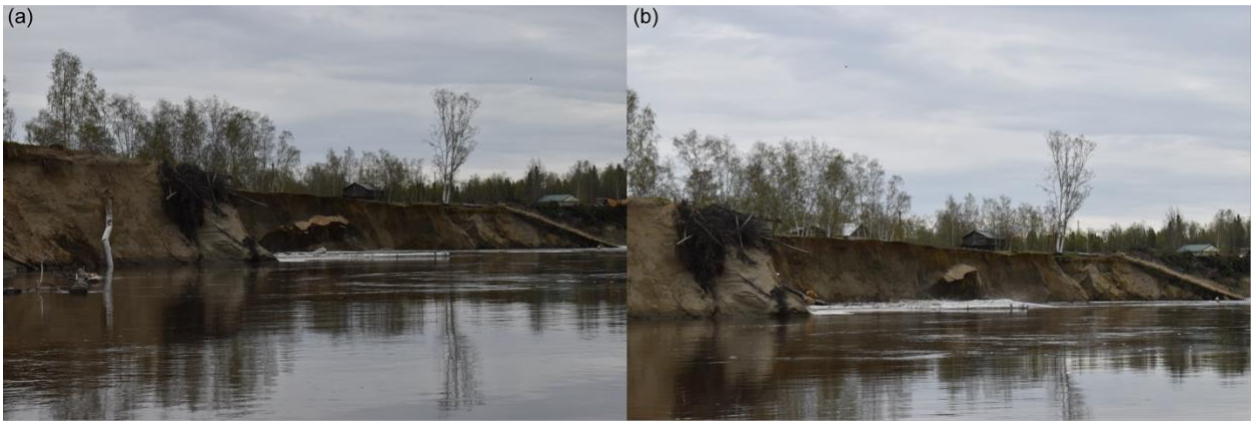


Figure S6: Photos of instantaneous bank collapse on the Koyukuk River at the upstream end of the town of Huslia, AK (65.6986111°, -156.3997222°). Multiple decameter-scale blocks of sediment collapsing into the Koyukuk River during the spring field season over the span of a few seconds. During this period, rapid bank erosion delivers a significant volume of sediment from the floodplain to the water column and riverbed.

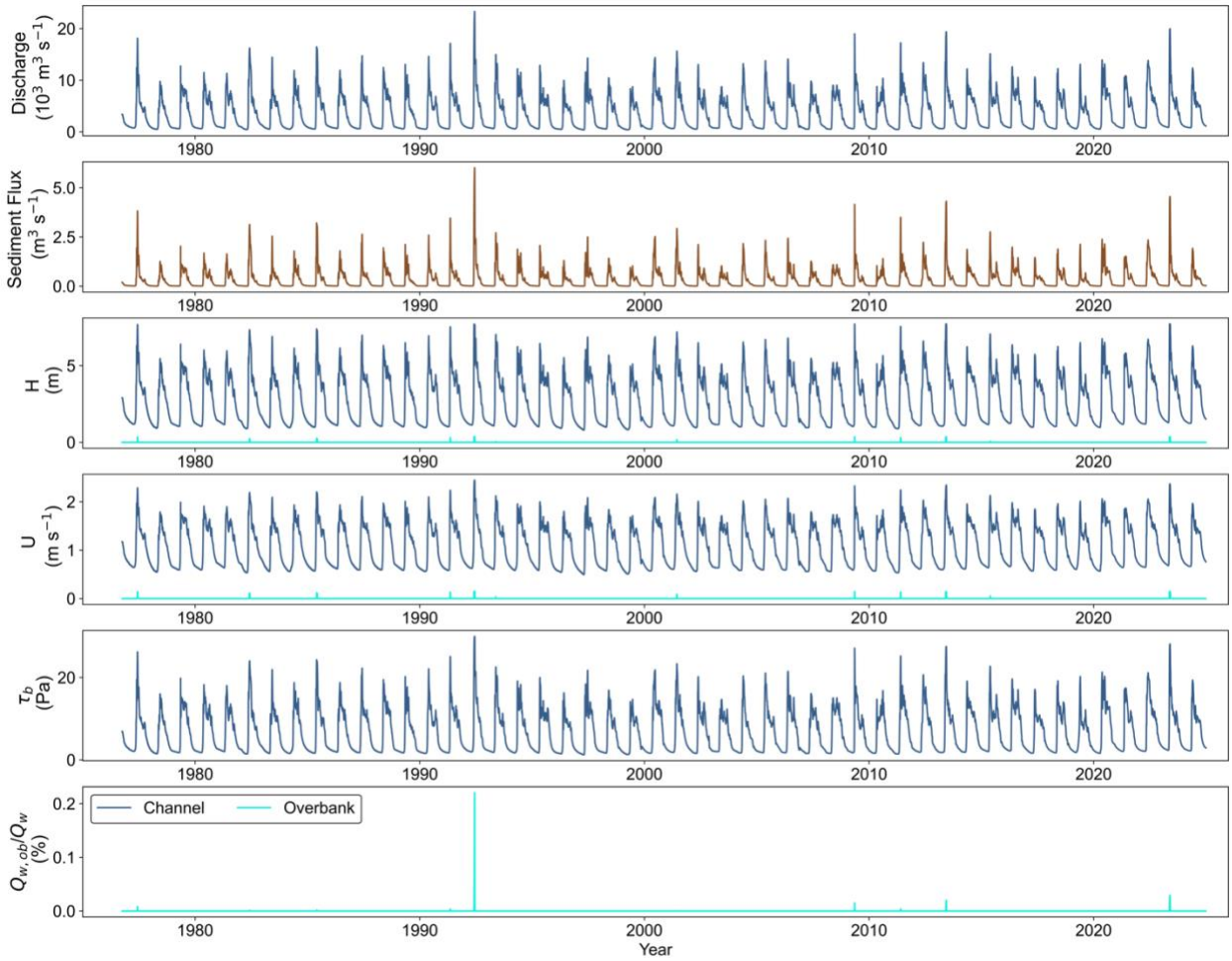


Figure S7: From the Stevens Village discharge record, we develop a time series of the sediment flux, in-channel and floodplain average depths and velocities, the in-channel bed shear stress, and the fraction of the total discharge conveyed by the floodplain.

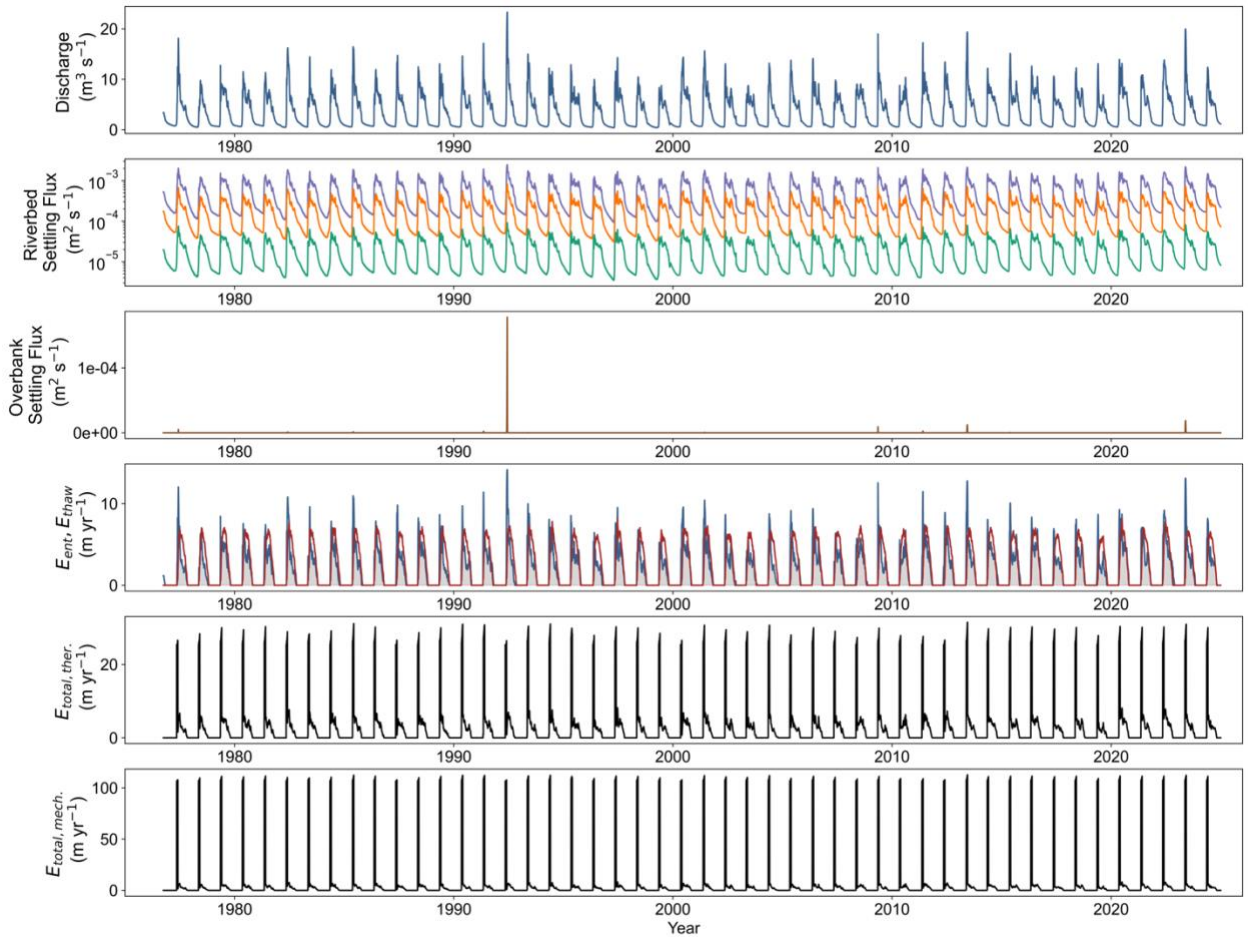


Figure S8: From the Stevens Village discharge record, we develop a time series of the sediment fluxes onto the riverbed and the top of the floodplain, as well as the lateral sediment flux entering the floodplain through point bar growth rate, which we assume to be equal to the bank erosion rate. For the riverbed, we delineate the sand (purple), mud (orange), and unflocculated mud (green) fluxes. For bank erosion, the modeled bank erosion rate (gray shaded region) is the minimum of the entrainment-limited rate (blue) and the thaw-limited rate (red) curves. Additionally, the modeled erosion rates for thermal and mechanical ice break-up endmembers are also presented.

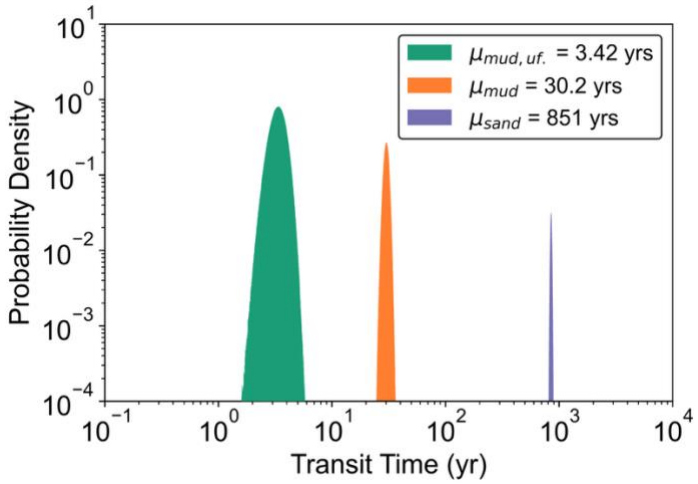


Figure S9: Simulated transit time distributions for unflocculated mud, flocculated mud, and sand particles experiencing only riverbed interactions. Details of the model are presented in the Discussion.

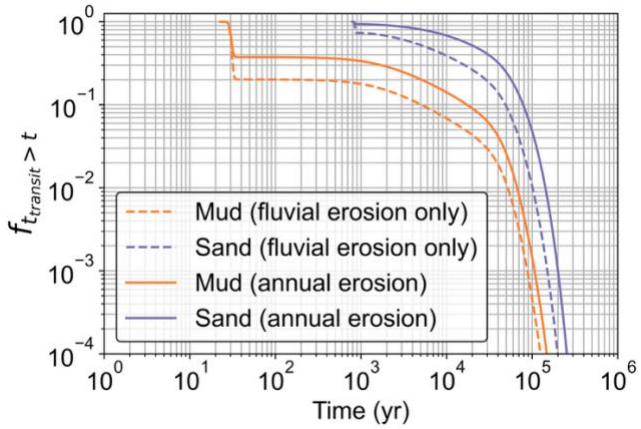


Figure S10: The fraction of simulated mud and sand transit times longer than time, t. The magnitude of the initial drop in each survivorship curve is the fraction of particles that never interacted with the floodplain. Following floodplain deposition, the transit time curves mirror the floodplain survivorship curve.

Site	Season	Year	Discharge [$m^3\ s^{-1}$]	Surface Concentration [$m^3\ m^{-3}$]
Huslia-DP-site	Winter	2025	1.16E+02	3.99E-06
Beaver-MainStem-DP-site	Winter	2025	7.63E+02	1.91E-06
Alakanuk-YukonMainStem-DP-site	Winter	2025		1.03E-06

Table S1: Sub-ice discharge estimates and surface suspended sediment concentrations measured in the winter of 2025.

Site	Season	Year	Discharge [m^3 s^{-1}]	Depth-Averaged SSC [m^3 m^{-3}]	Mud Fraction	Bed Mud Fraction	D_{50} [microns]	Bed D_{50} [microns]
Huslia-DP-site	Spring	2022	2050	0.000155	0.785	0.27	17.3	222.6
Huslia-DP-site	Fall	2022	1216	0.000059	0.682	0.26	24.3	240.7
Huslia-DP-site	Spring	2023	3197	0.00019	0.664	0.11	29.4	431.9
Huslia-DP-site	Fall	2023	1124	0.000039	0.824	0.17	16.9	342.2
Beaver-WideRiver-DP-site	Spring	2022	4667	0.000206	0.836	0.06*	19.3	
Beaver-MainStem-DP-site	Spring	2022	10271	0.000142	0.932	0.12*	12.3	
Beaver-MainStem-DP-site	Fall	2022	4879	0.000043	0.852		13.5	
Beaver-WideRiver-DP-site	Fall	2022	1783	0.000043	0.708	0.03*	24.6	
Beaver-MainStem-DP-site	Spring	2023	8762	0.000228	0.605	0.12*	40.3	
Beaver-WideRiver-DP-site	Fall	2023	1301	0.000027	0.897	0.09*	16.8	
Beaver-MainStem-DP-site	Fall	2023	5204	0.000039	0.807		16.1	
Alakanuk-YukonMainStem-DP-site	Spring	2023	8830	0.000426	0.788	0.59	29.2	48.8
Alakanuk-YukonMainStem-DP-site	Spring	2023	10364	0.000423	0.754	0.63	32.6	45.2
Alakanuk-YukonMainStem-DP-site	Fall	2023	6714	0.000253	0.935	0.1	10.8	205.1
Alakanuk-YukonMainStem-DP-site	Fall	2023	5892	0.000381	0.765	0.09	20.7	196.7
Alakanuk-AlakanukPassDownstr	Spring	2023	986	0.000669	0.567	0.18	49.5	171.1
Alakanuk-AlakanukPassMain-DP	Spring	2023	937	0.000698	0.696		31.4	
Alakanuk-AlakanukPassDownstr	Fall	2023	816	0.000252	0.918	0.09	10.8	227.2
Alakanuk-AlakanukPassMain-DP	Fall	2023	789	0.00024	0.941	0.08	10.9	238.1
Alakanuk-Kwiguk-DP-site	Spring	2023	2310	0.000497	0.569	0.08	48.9	308.3
Alakanuk-Kwiguk-DP-site	Fall	2023	1536	0.00022	0.95	0.06	9.9	335.4

Table S2: Suspended sediment data from our field surveys across the Yukon River Basin. We do not include riverbed D_{50} data for the Beaver samples because we did not sample the coarse grains. We did estimate the median bed grain size by performing a pebble count, the results of which are presented in Fig. S3. As described in the text, in Beaver, the bed mud fraction (denoted with an asterisk) was estimated from the measured grain size distribution and its estimated fraction of the total grain size distribution.

References

Bradley, R. W. and Venditti, J. G.: Reevaluating dune scaling relations, Earth-Science Reviews, 165, 356–376, https://doi.org/10.1016/j.earscirev.2016.11.004, 2017.

Douglas, M. M., Dunne, K. B. J., and Lamb, M. P.: Sediment Entrainment and Slump Blocks Limit Permafrost Riverbank Erosion, Geophysical Research Letters, 50, e2023GL102974, https://doi.org/10.1029/2023GL102974, 2023.

Fernandez Luque, R. and Van Beek, R.: Erosion And Transport Of Bed-Load Sediment, Journal of Hydraulic Research, 14, 127–144, https://doi.org/10.1080/00221687609499677, 1976.

de Lange, S. I., van der Wilk, A., Chassagne, C., Ali, W., Born, M. P., Brodersen, K., Hoitink, A. J. F., and Waldschläger, K.: Migrating subaqueous dunes capture clay flocs, Commun Earth Environ, 5, 729, https://doi.org/10.1038/s43247-024-01901-x, 2024.

Lauer, J. W. and Parker, G.: Modeling framework for sediment deposition, storage, and evacuation in the floodplain of a meandering river: Theory, Water Resources Research, 44, https://doi.org/10.1029/2006WR005528, 2008.

Partheniades, E.: Erosion and Deposition of Cohesive Soils, Journal of the Hydraulics Division, 91, 105–139, https://doi.org/10.1061/JYCEAJ.0001165, 1965.

Schiller, B. and Strom, K.: Entrainment of Muddy Sediment From Immobile Gravel River Beds, Water Resources Research, 62, e2025WR041519, https://doi.org/10.1029/2025WR041519, 2026.